

# Optical testing of the Far Ultraviolet Spectroscopic Explorer primary mirrors and predicted on-orbit performance

Raymond G. Ohl<sup>\*a</sup>, Scott D. Friedman<sup>a</sup>, Timo T. Saha<sup>b</sup>,  
Robert H. Barkhouser<sup>a</sup> and H. Warren Moos<sup>a</sup>

<sup>a</sup>Center for Astrophysical Sciences, Department of Physics and Astronomy,  
The Johns Hopkins University, Baltimore, MD 21218

<sup>b</sup>NASA/Goddard Space Flight Center,  
Greenbelt, MD 20771

## ABSTRACT

The Far Ultraviolet Spectroscopic Explorer (FUSE) is an astrophysics satellite designed to provide high resolution spectra ( $\lambda/\Delta\lambda = 24,000\text{--}30,000$ ) with large effective area ( $\sim 20\text{--}70\text{ cm}^2$ ) over the interval 90.5–118.7 nm. The FUSE instrument consists of four co-aligned, normal incidence, off-axis parabolic primary mirrors which illuminate separate Rowland circle spectrograph channels equipped with holographic gratings and delay line microchannel plate detectors.

We describe primary mirror surface metrology and compare experimental and theoretical vacuum ultraviolet (184.9 nm) imaging characteristics of the FUSE flight spare mirror, which has surface error characteristics similar to the actual flight units. The imaging performance of the flight spare was assessed in an autocollimation setup involving several flat mirrors and a tomographic imaging detector at the return beam focus. The Optical Surface Analysis Code (OSAC) software package was used to model image size from the double-pass test configuration based on figure error and surface roughness data. The model and experimental imaging data are in good agreement. Thus validated, we use the OSAC model to determine the image size associated with the flight spare mirror in single-pass. We conclude with a prediction of the on-orbit primary mirror point spread function in the FUSE bandpass and its impact on spectrograph slit transmission. We have achieved meaningful results with an inexpensive test program on an aggressive schedule.

**Keywords:** FUSE, optical testing, ultraviolet, scattering, imaging, off-axis parabola, OAP

## 1. INTRODUCTION

The Far Ultraviolet Spectroscopic Explorer (FUSE) is a NASA mission that will produce high resolution spectra ( $\lambda/\Delta\lambda = 24,000\text{--}30,000$ ) of astrophysical targets over the interval 90.5–118.7 nm utilizing a large effective area (20–70  $\text{cm}^2$ ). The FUSE wavelength range is rich in spectral lines arising from stellar and interstellar gas, providing the opportunity to make important contributions to many areas of astronomy. In particular, FUSE will measure the abundance of deuterium in a range of astrophysical environments to determine the extent to which stellar processing has modified the primordial abundance of deuterium — thereby providing a better understanding of the amount produced in the Big Bang and the subsequent change in abundance as the universe aged.

The instrument consists of four normal incidence, off-axis parabolic mirrors, which are co-aligned and illuminate separate Rowland circle spectrograph channels with holographically ruled gratings (Figure 1).<sup>1,2</sup> Two microchannel plate detectors with delay line anodes each record spectra from a pair of optical channels.<sup>3</sup> This scheme of four independent UV optical paths allowed us to tailor optical coatings to maximize instrument effective area in the bandpass.

Each primary mirror has a rectangular,  $387.0 \times 351.8$  mm aperture and 2245 mm focal length with  $5.5^\circ$  off-axis angle (Figure 2a).<sup>4</sup> The four mirror substrates are identical, with the proper off-axis section set by an aperture

---

\* Also at Astronomy Department, University of Virginia, P.O. Box 3818, Charlottesville, VA 22903  
Correspondence: Email: ohl@pha.jhu.edu; <http://fuse.pha.jhu.edu>; Telephone: 410 516 4375; Fax: 410 516 5494

stop located near each mirror surface (slightly different off-axis sections are dictated by the grating incidence angles required to optimize the spectrograph channels for two wavelength bands). The two inside corners of each mirror are masked to match the grating apertures, whose outside corners were removed to satisfy space constraints. The resulting geometric area of each mirror is approximately 1330 cm<sup>2</sup>. The apertures are widely separated on the instrument optical bench, resulting in four parallel and separated optical axes.

The mirrors are made from Zerodur, which was chosen for its low coefficient of thermal expansion (CTE). The blanks were aggressively weight-relieved: 70% of the substrate material was removed from each, leaving a triangular isogrid rib pattern with a 7.5 mm-thick facesheet and a final weight of  $\sim$  17 lb. (Figure 2b). SVG Tinsley Laboratories (“Tinsley”) lightweighted the blanks and figured the mirrors into parabolas.\*

Two mirrors are coated with ion beam sputtered silicon carbide (SiC) and two are coated with lithium fluoride (LiF) over aluminum, to maximize reflectivity from 90.5–110.3 nm and 98.0–118.7 nm, respectively. The Optical Thin Film Laboratory at NASA/Goddard Space Flight Center (GSFC) applied all of the coatings for the FUSE mirrors.

The instrument optical bench is composed of a graphite/cyanate ester composite material, designed to have a high strength-to-weight ratio, low CTE, and to insure dimensional stability over long integrations ( $\sim$  200 kilo-second). However, mechanical G-release, thermal expansion, and moisture desorption are expected to change the structure’s dimensions significantly upon orbital insertion and slowly over the life of the satellite. Errors in the placement of the mirror assemblies on the instrument optical bench further misalign the mirrors with respect to the spectrograph.<sup>5</sup> Each mirror is therefore equipped with precision actuators that permit independent tip, tilt, and focus control for on-orbit alignment (Figure 2d). Each mirror is mounted with three flexures to its own composite sandwich plate, which isolates the mirror from stress induced by adjustments of the actuators. The flexures are oriented with soft axes radial to the center of the mirror (Figure 2b), and consist of titanium alloy blades attached to low-CTE Invar fittings (Figure 2c). Each Invar fitting is bonded to a mirror rib.

In addition to meeting reflectivity specifications,<sup>6</sup> the fully assembled primary mirrors have the following imaging requirement: The mirrors must have 90% encircled energy (EE) at 100.0 nm in a diameter of 1.5 arcsec, which corresponds to 16  $\mu$ m diameter at the focal plane. In order to meet this requirement, we established fabrication tolerances based on SOHO SUMER<sup>†</sup> mirror heritage<sup>7</sup> and a modulation transfer function (MTF) analysis carried out at The Johns Hopkins University (JHU). The surface fabrication specifications are as follows: figure error better than  $\lambda/40$  RMS and  $\lambda/10$  peak-to-valley (P-V) at  $\lambda = 632.8$  nm; midfrequency error less than 20 Å RMS over 10.0–0.1 mm spatial scales; and microroughness less than 10 Å RMS over 100–1  $\mu$ m. These specifications were validated by an independent analysis.<sup>8</sup> This performance insures adequate transmission through the 1.25  $\times$  20 arcsec, high-resolution spectrograph slit and could impact instrument spectral resolution when using wider slits.

In summary, we designed primary mirror assemblies that were lightweight and adjustable in three degrees of freedom, maximized instrument effective area in the bandpass, and met a stringent imaging requirement. In this paper, we discuss optical testing and modeling of the FUSE primary mirrors toward a prediction of the on-orbit mirror point spread function (PSF) and its impact on spectrograph slit transmission. We use the Optical Surface Analysis Code (OSAC)<sup>7,9</sup> at GSFC to model visible to far-ultraviolet (far-UV) imaging of the flight spare mirror (“spare”) in double- and single-pass, based on surface metrology. This model was validated with laboratory double-pass imaging data from the spare at 184.9 nm.

This test program was completed under a tight budget and aggressive schedule. The image test was not meant to fully characterize the performance of the telescope mirrors in the FUSE bandpass. Rather, it was designed to insure that there were no severe problems with the flight mirrors and the implications of surface metrology data were understood. The test produced a data set which we used to validate our modeling and extrapolate a prediction into the FUSE bandpass with confidence. The interpretation of our laboratory results therefore relies heavily on optical analysis tools developed for previous UV and X-ray space astronomy missions.

---

\*Silicon Valley Group, Inc., Tinsley Division, Tinsley Laboratories, Richmond, California.

<sup>†</sup>Solar Ultraviolet Measurements of Emitted Radiation experiment on the Solar Heliospheric Observatory.

## 2. OPTICAL SURFACE ANALYSIS CODE

There are three components to the on-axis image size produced by the FUSE telescope mirrors: aperture diffraction, geometric broadening, and scattering.<sup>10</sup> Aperture diffraction arises from the interaction of the incoming wavefront with the edges of the mirror entrance pupil. Geometric image broadening results from rays misdirected by departures from an ideal, parabolic surface (i.e. departures with large spatial period — not amplitude — across the mirror surface). The scattering component can be regarded as wavefront diffraction from small-spatial period mirror surface errors.

One can best describe the modeling presented here in terms of boundaries on the spatial period of mirror surface errors important to the geometric and scattering components of image broadening: figure error ( $> 60$  mm), mid-frequency error (60–1 mm), and microroughness ( $< 1$  mm). We have ascribed geometric broadening of the PSF to figure errors via a “raytrace” calculation, while counting the smaller-scale, mid-frequency errors and microroughness as contributing to scattering. At far-UV wavelengths, mid-frequency errors are very important to the shape of the PSF. They remove energy from the core produced by aperture diffraction and geometric broadening and displace it to form broad wings at larger radii. The wavelength and spatial scale of interest at the focal plane determines which features one assigns to a raytrace calculation and which to a scattering calculation. For example, surface errors with a 60 mm spatial period scatter light to a circle about 0.8 arcsec in diameter for  $\lambda = 120$  nm.

The OSAC model of the FUSE mirror requires four inputs: The basic shape of the optic (off-axis paraboloid), aperture geometry for the aperture diffraction calculation, figure error for the raytrace calculation, and the power spectral density (PSD) of surface errors for the scatter calculation. The PSD for the spare is displayed in Figure 4. For the purposes of the scatter calculation, OSAC assumes small-scale surface errors are isotropic. OSAC essentially creates a two-dimensional function for each of the three imaging components listed above and convolves them for a final PSF. The capabilities and scattering physics associated with this version of OSAC are fully described elsewhere.<sup>7,11</sup>

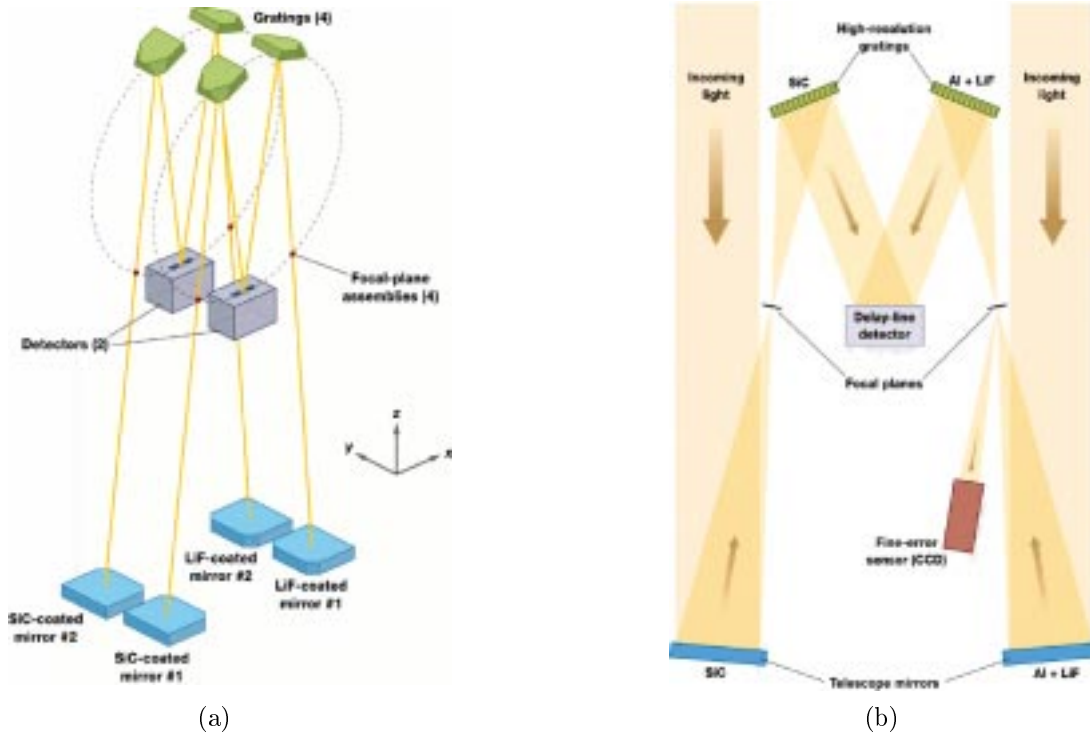
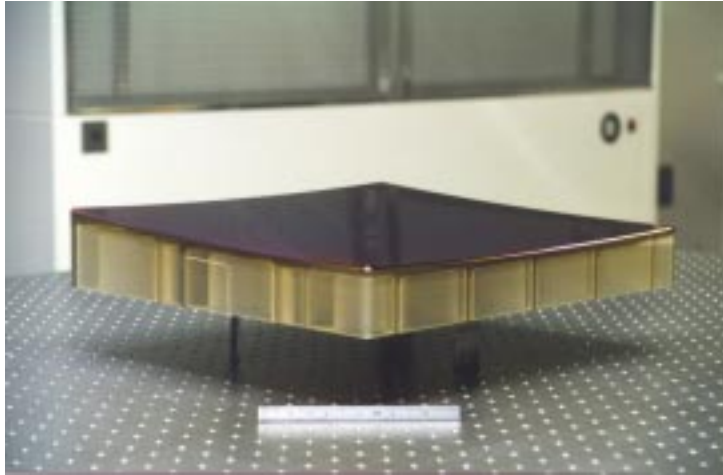
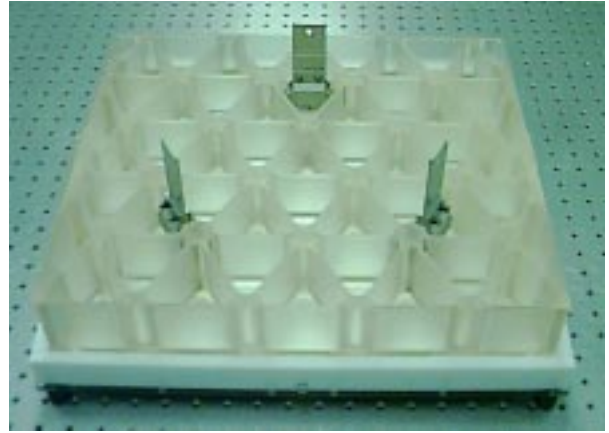


**Figure 1.** (a) Schematic diagram of FUSE optical design (four UV optical paths, each pair sharing one detector). (b) Sketch showing collimated light entering one side of the FUSE instrument, tracing two UV optical paths, and entering a visible-light Fine Error Sensor camera.



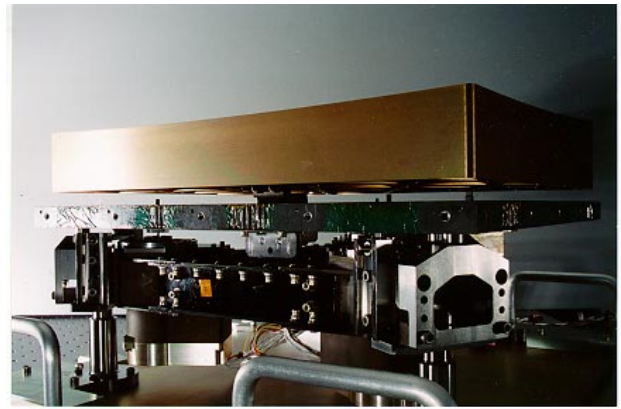
(a)



(b)



(c)



(d)

**Figure 2.** (a) FUSE mirror resting face-up on flexures. (b) FUSE mirror resting face-down, showing lightweighting and flexures. (c) Close-up of titanium blade flexure pinned to Invar fitting which is bonded to the mirror rib. (d) FUSE mirror assembly (actuators, composite plate, and mirror substrate; here with dummy, aluminum “mirror”) shown from the side, attached to a handling plate (photo credit: Swales and Associates, Inc., Beltsville, Maryland). Vertex of the parent paraboloid is to the bottom right of the mirror surface in frame a and to the top of frame b.

### 3. SURFACE METROLOGY

#### 3.1. Figure Measurements

Interferometric figure measurements were made at Tinsley during mirror fabrication and at JHU throughout assembly build-up. Tests were performed at JHU in a double-pass autocollimation setup employing a He-Ne (632.8 nm) laser unequal path interferometer (LUPI).<sup>‡12</sup> Details of the test and alignment method are discussed elsewhere.<sup>13</sup> The LUPI sends a collimated beam into a diverging lens with focus at the flight mirror focal point. The beam is collimated by the parabolic flight mirror and returned by a 21 in. diameter flat mirror with  $\lambda/20$  P-V figure error and 2.3 Å RMS microroughness.<sup>§</sup> During the test, the flight mirror is supported at two points optimized to help minimize gravitational distortion.<sup>4</sup> The mirror also leans very slightly against three back support points. The attached mirror assembly hardware is off-loaded during the test. For each figure test, alignment was accomplished via analysis of static interferograms: The wavefront error was minimized as a function of relative alignment of the LUPI, autocollimating

<sup>‡</sup>Buccini Instrument Co., Wilmington, North Carolina.

<sup>§</sup>Nu-Tek Precision Optical Corporation, Aberdeen, Maryland fabricated the autocollimating flat. The effect of the flat’s surface error on the far-UV wavefront in the 184.9 nm image test is not included in the OSAC modeling (Section 5).

flat mirror, and flight optic under test. The figure tests performed at Tinsley with a phase-shifting interferometer agreed well with the JHU results.

Tinsley delivered flight mirrors that met the figure fabrication specification ( $0.025\lambda$  RMS), in spite of distortion attributable to epoxy-induced stress at the mirror blade flexure bond-line (Figure 2c).<sup>14</sup> For all four flight mirrors and the spare, the final RMS figure error after assembly build-up at JHU is about a factor of 2 worse than the fabrication specification ( $\sim 0.050\lambda$  vs.  $0.025\lambda$ ; Table 1). This increase in figure error is caused by assembly-induced strain.<sup>14</sup> Raytrace modeling and a MTF analysis performed at JHU indicated that this increased figure error would primarily broaden the image core, and would not adversely affect the EE performance at a diameter of 1.5 arcsec at 100.0 nm. We accepted this increased RMS figure error based on this analysis and the cost and schedule impact associated with obtaining a lower RMS figure error for the fully-assembled mirrors.

An optical path difference (OPD) surface plot of the typical figure error for a fully assembled flight mirror is shown in Figure 3. A “Y-shaped” ridge,  $> \lambda/10$  high, is oriented through the mirror flexures with the shank of the “Y” pointed toward the mirror vertex. Superimposed on this ridge feature over each flexure location are three depressions about  $< \lambda/10$  deep and  $\sim 2$  cm wide.

The PSDs displayed in Figure 4 from figure data fall off at lower spatial frequencies because they were calculated after low frequency features were removed via a 37-Zernike polynomial fit to the OPD surface map (for OSAC raytrace analysis). The shelf in the Tinsley figure PSD around  $\text{Log}_{10}\nu \simeq -1$  is an artifact associated with spurious reflections in the Tinsley interferometer. The JHU figure measurement suffers from reduced spatial sensitivity, so the associated PSD drops off faster than the Tinsley figure data at high frequencies.

### 3.2. Mid-Frequency Measurements

Tinsley made interferometric measurements of mid-frequency error prior to mirror delivery. They sampled several 10 mm diameter patches on each mirror, measuring surface errors over 10–0.1 mm spatial periods with amplitude sensitivity  $\sim 1 \text{ \AA}$  (Table 1).

We verified the Tinsley measurements with Bauer Model 100 profiler data obtained at GSFC on two of the mirrors.<sup>15</sup> The Bauer profiler is sensitive to amplitudes  $\sim 1 \text{ \AA}$  with 10–0.5 mm spatial periods. The Bauer results (not shown) fall significantly below the Tinsley mid-frequency PSD in Figure 4. However, the Tinsley curve is based on only one of several measurement locations on the spare, while Bauer measurements were made at many different locations on the mirror. For the purposes of this modeling, the more conservative Tinsley measurement was used. More data reduction and interferometric measurements at GSFC to be completed in the near future should resolve this issue.

### 3.3. Microroughness Measurements

Measurements of microroughness (not displayed) were performed at Tinsley with  $\sim 1 \text{ \AA}$  amplitude sensitivity over 100–0.4  $\mu\text{m}$  spatial periods (Table 1). The model fit to the figure and mid-frequency PSD data shown in Figure 4 agrees well with the Tinsley microroughness data when extrapolated to higher spatial frequencies.

## 4. IMAGE TESTING

We present measurements of the double-pass imaging performance of the spare in an autocollimation setup at  $\lambda = 184.9 \text{ nm}$ . The spare is similar to the fully assembled flight units in terms of figure error and surface roughness (Table 1), so imaging data gathered with the spare are indicative of flight mirror performance. We designed this test to ensure there were no gross problems with the flight mirrors, to give a qualitative picture of the shape of the mirror PSF, and to provide quantitative data with which to validate OSAC modeling based on surface metrology.

The test setup is shown schematically in Figure 5. It is essentially the same arrangement used for measurements of figure error during flight mirror assembly (Section 3.1). The setup was aligned interferometrically before proceeding with the image test. The UV source, a mercury (Hg) pencil lamp, and pinhole aperture are offset from the spare’s nominal focus in (folded) -Z and +X by 12.7 mm and 2.54 mm, respectively. This offset produced no significant increase in spot size<sup>¶</sup> and sent the return beam into the knife edge (KE) detector. The optical path was purged with  $\text{N}_2$  to facilitate testing at 184.9 nm.

---

<sup>¶</sup>A ZEMAX raytrace assuming a perfectly parabolic mirror with this offset from nominal focus gives a RMS spot radius of 0.56  $\mu\text{m}$ , which is much less than the broadening expected from, e.g., figure error.

### SiC2 Final Figure Test (Full Assembly)

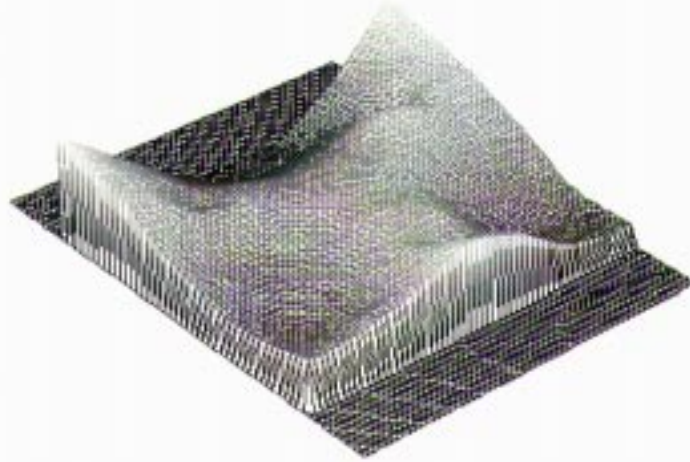


**Figure 3.** Optical path difference surface map of a typical flight mirror with  $\sim 0.050\lambda$  RMS figure error ( $\lambda = 632.8$  nm). Note “Y-shaped” distortion. Vertex of the parent paraboloid is to the bottom right of the surface plot.

We used the KE detector to obtain the two-dimensional energy distribution at the return beam focus. The spot is directed into a narrowband filter (184.9 nm) and UV-sensitive photomultiplier tube (PMT). The KE is translated through the beam in the plane perpendicular to the optical axis and in the direction normal to the KE. The signal from the PMT is recorded as a function of KE position. The negative derivative of the resulting knife edge distribution (KED) is the line spread function (LSF; Figure 6). Ideally, a LSF is a one-dimensional cut through the spot convolved with a line source placed parallel to the KE. Best focus is found by minimizing the width of a Gaussian fit to the LSF for KE scans taken in X at different focal positions. The KE is then rotated about the optical axis to scan through the return spot from another azimuthal angle in the focal plane, and another LSF is generated. Given infinite angular sampling in this manner, an infinitely small KE step size, and an infinitely large signal-to-noise ratio, an image of the energy distribution in the focal plane can be nearly perfectly reproduced via tomographic algorithms. We employed a filtered back-projection algorithm (a discrete approximation to the inverse Radon operator).<sup>16</sup>

After obtaining LSF data at 8 angles in the focal plane, we performed synthetic encircled energy (EE) measurements on the reconstructed spot (Figure 7). Although artifacts from discrete angular sampling appear in the reconstruction, they tend to cancel, because the synthetic aperture photometry is azimuthally averaged. EE measurements made on the reconstructed image are therefore very close to the ideal measurement (i.e. differences between EE measurements performed on a perfect synthetic image and the corresponding image with reconstruction artifacts are  $\ll 5\%$ ). We used a KE step size of  $5 \mu\text{m}$  when scanning across the spot. This step size smoothed the image, but did not significantly change the spot width.

The tomographic EE data were of high quality only for diameters  $< 4.6$  arcsec ( $< 50 \mu\text{m}$  at the focal plane). No measurements of wide-angle scatter were made (i.e. at diameters of order 100 arcsec). With no careful laboratory measurement of the total spot energy, the normalization of the tomography EE data is based on the EE function generated by the OSAC model.

Direct encircled energy measurements were also made by replacing the knife edge in front of the PMT with pinhole apertures of 10, 40, and  $200 \mu\text{m}$  diameter and peaking up the PMT signal by translating in three axes (Figure 7). The normalization for these measurements was based on the signal within the large,  $200 \mu\text{m}$  pinhole. This check agreed well with the EE data generated by the tomography technique outlined above.

There are many systematic effects that potentially contribute to broadening or other distortion of the detected spot size for the image test setup and tomography scheme:

1. Vibration. Crude interferometric measurements of mechanical vibration in the setup show a maximum amplitude of about  $< 0.1$  arcsec for frequencies  $< 10$  Hz.<sup>13,17</sup> In addition, early tomographic KE tests

at 632.8 nm of a flight mirror with RMS figure error of  $\sim 0.030\lambda$  imaged a spot clearly dominated by aperture diffraction, indicating vibration is a negligible effect.

2. Atmospheric turbulence. Turbulence along the optical path was essentially eliminated by controlling the cleanroom air flow and temperature gradients during testing.<sup>13</sup> However, working at the vacuum UV wavelength 184.9 nm required purging the setup with N<sub>2</sub>, the active introduction of which caused a great deal of turbulence. We mitigated this problem by shutting off the N<sub>2</sub> flow, allowing the test chamber to stabilize before beginning each KE scan, and purging again between scans.
3. Lamp stability. We found the output of the Hg lamp to be stable to  $\ll 1\%$  over time periods relevant to a given KE scan ( $\sim 5$  min.). This effect was therefore not a significant source of image broadening.
4. Beam non-uniformity. We mounted the PMT at the location of the system entrance pupil and translated it in X and Y to map out the energy distribution in the beam. The beam was found to be uniform to  $\sim 5\%$ . Out-of-focus KE scans are also consistent with a uniform pupil illumination.
5. Red leak. Measurements of the relative response of the filter-PMT combination at 184.9 and 253.7 nm were made using a monochromator with known grating efficiency. About 5% of the PMT signal during this image test is from light associated with the Hg line at 253.7 nm. Although scattering is less important at 253.7 nm compared to 184.9 nm, the main factor in determining the image size for these data is figure error, which is constant with wavelength. This red leak is therefore not important to the image size detected with this test. The visible response of the filter-PMT system is negligible.
6. Flat mirrors. Surface errors on the flat mirrors in the test setup distort the UV wavefront. We measured the figure and mid-frequency error and microroughness of the two small folding mirrors at GSFC using the Bauer profiler and a Wyko TOPO 3-D interferometer.<sup>||</sup> The small flats have almost negligible surface error compared to the spare on all spatial scales. Although it has excellent figure and microroughness characteristics (Section 3.1), the mid-frequency error on the large flat was not measured. Since this flat was ion-polished, mid-frequency error may be a concern.
7. Pinhole source size. The 10  $\mu\text{m}$  diameter pinhole source aperture is mounted at  $45^\circ$  to the outgoing beam. The finite thickness of the pinhole substrate causes the source to appear “slit-like,” essentially presenting a  $1 \times 6 \mu\text{m}$  slit in object space, as verified by visual inspection with a microscope. The proximity of the Hg lamp to this aperture during the test implies that the slit is essentially uniformly illuminated during the test.
8. Alignment drift. Before beginning an image test, system alignment was achieved with the LUPI and a figure test was performed to ensure the mirror figure was stable (Section 3.1).<sup>14</sup> Afterward and over the course of the image test, the spare tended to rotate out of alignment about its support points at  $\sim 15$  arcsec per hour (i.e. rotating about the horizontal axis, producing vertical tip misalignment). This drift slowed with time and an attempt was made to correct for it over the course of the image test. A less severe drift in rotation about the vertical axis was also observed. The primary effect of the drift was to add coma and defocus to angles that were sampled later in the image test, changing their shape and thus warping the final, reconstructed image.

The last two effects listed above alter image size and structure, but experimentation with the OSAC model indicates that they do not overwhelm the effect of mirror figure error (Section 5.1).

## 5. MODEL VALIDATION

The OSAC model of the image test setup includes only the spare mirror sampled in double-pass. The surface error on the small flat mirrors and the figure error and microroughness on the large flat are almost negligible compared to the spare. Although the mid-frequency error on the large flat is not known, we have obtained results without including a scattering component from this optic in the model.

---

<sup>||</sup>Veeco Instruments Inc., Veeco Metrology Group, Wyko Optical Profilers, Tucson, Arizona.

### 5.1. Tomographic Encircled Energy Data

Two orthogonal laboratory KEDs and derived LSFs for the spare and LSFs from the OSAC model prediction are displayed in Figure 6 (X and Y). The associated EE curves are shown in Figure 7.

System alignment is a major factor in the shape of these LSFs and EE curves. In order for the OSAC predictions to match the observed return spot, rough estimates of the amount of tilt misalignment and defocus were added to the model: 7 arcsec of mirror rotation about the X-axis and 45 arcsec of rotation about the Y-axis were added. The magnitude of the rotations were consistent with that expected from measurements of alignment drift. 45  $\mu\text{m}$  of defocus was also added (i.e. relative to the nominal focus, 2245 mm from the mirror vertex). The amount of defocus was consistent with the error in focus during the image test. The spot consists primarily of a tight “core” and broad “shoulder.” Raytrace calculations show the shoulder arises from light which hits the “Y-shaped” distortion on the mirror (Figure 3). These two components shift relative to each other in X for different focal positions. The focus for a given test was chosen to minimize the size of the core in X via a Gaussian fit and to place most of the shoulder on one side of the core. Note that the alignment drift also changed the focus for angles sampled later in the test by translating the mirror vertex away from the laboratory mount. This complicated the choice of defocus for the modeling.

OSAC modeling of a mirror with perfect figure in the same orientation indicates that the effect of figure error on spot size and structure is well-detected behind the given amount of misalignment and defocus.

Many angles were sampled for the tomography algorithm and the optical path was purged with  $\text{N}_2$  between scans (Section 4). As the test wore on (many hours), the setup became more misaligned and defocused (see above). So the LSFs taken later in the test have power in areas not predicted by the amount of misalignment and defocus assumed for the OSAC prediction. (The OSAC prediction was tuned in terms of misalignment and defocus to match the X and Y LSFs — the first two LSFs to be taken during a test). This is the reason the experimental EE points and theoretical curve in Figure 7 disagree somewhat for diameters 25–35  $\mu\text{m}$  — there is a misallocation of power in LSFs for angles measured at later times during the image test.

A uniformly illuminated  $1 \times 6 \mu\text{m}$ , rectangular slit source has been assumed for the model. Minor deviations of the data from the model near the center of the LSFs displayed in Figure 6 could be attributed to uncertainties in the precise shape of the slit source and the distribution of light within and around this aperture (e.g. scattered light from the edges), as well as unaccounted for misalignment and defocus.

The JHU image test data are consistent with OSAC predictions, given the systematic effects discussed above. The disagreement is at most  $\sim 5\%$  in EE at any given diameter.

### 5.2. Additional Encircled Energy Data

EE measurements were also obtained at 184.9 nm by peaking up on the return beam with pinhole apertures (Figure 7). These measurements agree well with the OSAC EE predictions and the EE results from the tomographic image test. The  $1\text{-}\sigma$  error from photon statistics associated with these numbers is  $< 1\%$ . Systematic effects are very important when comparing these numbers to the 184.9 nm EE data. The most important effects are the choice of focus (Z) and X and Y centering of each pinhole aperture. The error bars shown for these data in Figure 7 roughly estimate the effect of this systematic uncertainty.

### 5.3. Limits on the Model Validation

Though the encircled energy data presented above agree well with the OSAC model predictions, the comparison is more relevant to the accuracy of the figure model than the scatter calculation. In this double-pass setup, sampled at 184.9 nm, scattering removes about 17% of the total spot energy from the core produced by figure error and aperture diffraction and spreads it to larger radii. Since the tomographic EE data have reliable signal-to-noise ratio only for diameters  $< 4.6$  arcsec ( $< 50 \mu\text{m}$ ), scattered energy was not measured at positions outside this diameter. Mirror surface errors with spatial period greater than about 16 mm scatter energy within this diameter. Furthermore, given the image smoothing associated with the finite KE step size and the extended slit source, the effect of scattering to these smaller diameters is not well-detected.

The  $\sim 0.050\lambda$  RMS figure distortion gives rise to a geometric component to mirror imaging which is important to the shape of the EE curve for diameters  $< 1.5$  arcsec and to the energy distribution within the width of the narrow, high-resolution spectrograph slit ( $1.25 \times 20$  arcsec). The spare is very similar to the flight mirrors in the magnitude

and character of figure error (Table 1 and Figure 3). The data from this laboratory image test was important to the development of the correct figure error component to the OSAC model, which is critical for predicting the shape of the PSF within and near the edges of the narrow slit.

## 6. OSAC PREDICTION

### 6.1. Single-Pass OSAC Prediction

Predicted single-pass EE curves at 633.0 and 100.0 nm are shown in Figure 8. Synthetic apertures were centered on the centroid of image intensity at best focus. Aperture diffraction makes the EE curve for 633.0 nm broader than the 100.0 nm curve for some diameters. The EE curve at 100.0 nm is about 1.5% below the specification of 90% EE within a diameter of 1.5 arcsec. The additional, assembly-induced figure error is the main factor in broadening the core of the PSF, dropping the EE curve at 100.0 nm slightly below the requirement.

There are two sources of uncertainty in the OSAC prediction. The first is the uncertainty in the input PSD for the scatter calculation (Figure 4). The Tinsley mid-frequency measurement is about an order of magnitude worse than data at the same spatial frequencies obtained at GSFC (Section 3.2). If the GSFC results are accurate, the 100.0 nm EE curve would improve by about 1% at 1.5 arcsec diameter.

The second source of uncertainty arises from the OSAC approximation to short-wavelength scattering physics. Previous studies indicate an error of about  $< 5\%$  for regions of the EE curve dominated by scatter.<sup>7,18</sup>

### 6.2. On-Orbit Performance Prediction

The on-orbit spot consists of the mirror PSF convolved with a function describing FUSE spacecraft jitter. Using our forecast of in-flight jitter (0.5 arcsec FWHM), the prediction for transmission through the  $1.25 \times 20$  arcsec slit is  $87 \pm 5\%$  at 100.0 nm. The quoted error is a rough estimate of the effect of the systematic errors in the OSAC prediction mentioned previously. This slit transmission is sensitive to the severity of spacecraft jitter. An improved pointing accuracy of 0.25 arcsec FWHM would increase the slit transmission by about 4%. The instrument-level requirement for  $1.25 \times 20$  arcsec slit transmission, including the effect of jitter, is 50%.

Similarly, the predicted transmission for the mid-resolution,  $4.0 \times 20$  arcsec slit is  $96 \pm 5\%$  at 100.0 nm. This value is less sensitive to reasonable assumptions about spacecraft jitter. The requirement for the minimum transmission through this slit, including jitter, is 95%. These slit transmissions do not include the effect of image broadening from misalignments of the mirror assemblies on the instrument optical bench. Our analysis indicates that the primary mirrors will meet the instrument-level specifications for slit transmission for both the  $1.25 \times 20$  and  $4.0 \times 20$  arcsec apertures.

For areas of the spectrum not limited by detector performance, the on-orbit spot should improve instrument spectral resolution over the performance observed during spectrograph alignment at the University of Colorado.<sup>19</sup>

## 7. CONCLUSION

Based on surface metrology and validated with laboratory image testing of the spare, modeling indicates that the mirrors will have about  $89 \pm 5\%$  EE at 100.0 nm, where the quoted error is a rough estimate of uncertainties in the metrology data and modeling, and real variations from mirror to mirror. The mirrors will therefore meet or come very close to meeting their imaging specification. This prediction translates into an estimate for on-orbit,  $1.25 \times 20$  arcsec slit transmission that is dependent on spacecraft pointing.

Schedule constraints prevented image testing the flight mirrors as originally planned. However, image testing was meant to confirm the far-UV performance implied by surface metrology. Testing the flight spare mirror longward of the FUSE bandpass placed tight limits on the impact of figure error on imaging and very coarse limits on the effect of short-wavelength scattering. Since the spare has surface error similar to the fully assembled flight mirrors, this test was sufficient to verify that there are no severe problems with the flight mirrors and, in combination with OSAC modeling, confirmed our performance expectation based on surface metrology.

We have successfully completed a fast, inexpensive optical test program for the FUSE primary mirrors. The development of modern analysis tools for understanding optical performance in the far-UV for other space astronomy missions has been critical to the complete interpretation of our results.

For more information about the mission, see the FUSE web home page at: <http://fuse.pha.jhu.edu>.

**Table 1.** Assembled Flight Mirror RMS Surface Error.\*\*

Mirror:	(spec.)	Spare	SiC1	LiF1	SiC2	LiF2
Figure ( $\lambda = 632.8$ nm):	$0.050\lambda$	$0.047\lambda$	$0.047\lambda$	$0.051\lambda$	$0.045\lambda$	$0.048\lambda$
Mid-frequency ( $\text{\AA}$ ):	20	$11.8 \pm 1.2$	$12.5 \pm 1.6$	$14.1 \pm 1.8$	$11.6 \pm 1.9$	$18.5 \pm 4.4$
Microroughness ( $\text{\AA}$ ):	10	$3.7 \pm 1.4$	$3.7 \pm 1.1$	$6.4 \pm 1.4$	$4.8 \pm 0.6$	$9.8 \pm 2.3$

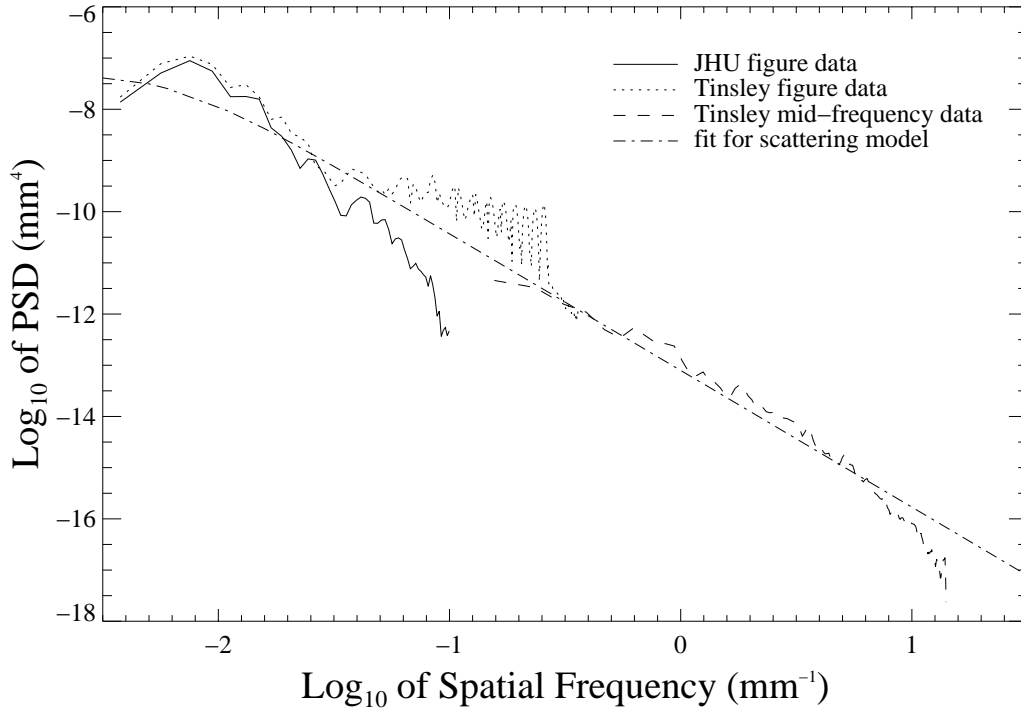


**Figure 4.** Two-dimensional power spectral density (PSD) of mirror surface error for the flight spare mirror (microroughness is not shown). The model fit for the OSAC scattering calculation is also displayed.

### ACKNOWLEDGMENTS

The authors gratefully acknowledge Daniel Carrigan, formerly of Swales and Associates, Inc., for his hard work during the demanding assembly and test phases of the mirror program and Dr. David Content of NASA/Goddard Space Flight Center for his assistance in measuring mirror surface error. This work is supported by NASA contract NAS5-32985.

---

\*\*RMS figure error values are based on measurements at JHU prior to integration of the fully assembled flight units with the rest of the instrument. Each figure measurement is uncertain to  $\sim 0.005\lambda$ . RMS mid-frequency and microroughness values quoted here were derived by Tinsley from measurements made before delivery to JHU. Tinsley sampled each mirror at several locations. These numbers are the average measurements from each data set, and the listed “error” is the 1- $\sigma$  spread in values.

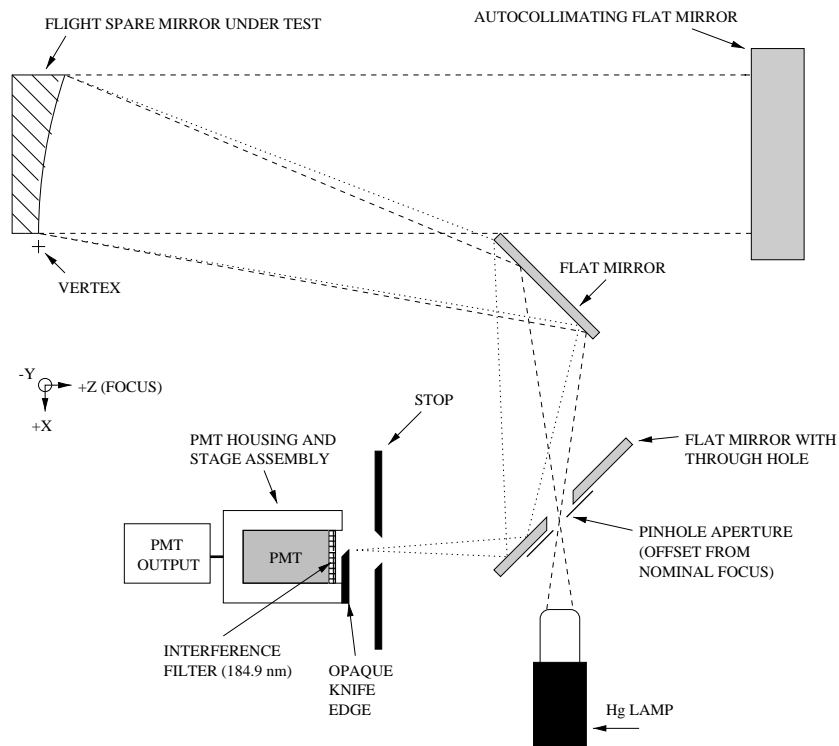


**Figure 5.** Schematic of the image test setup in the class 10,000 cleanroom laboratory at JHU (not to scale). All hardware was attached to a vibrationally isolated optical bench and surrounded by a  $N_2$  purge enclosure for testing at 184.9 nm.

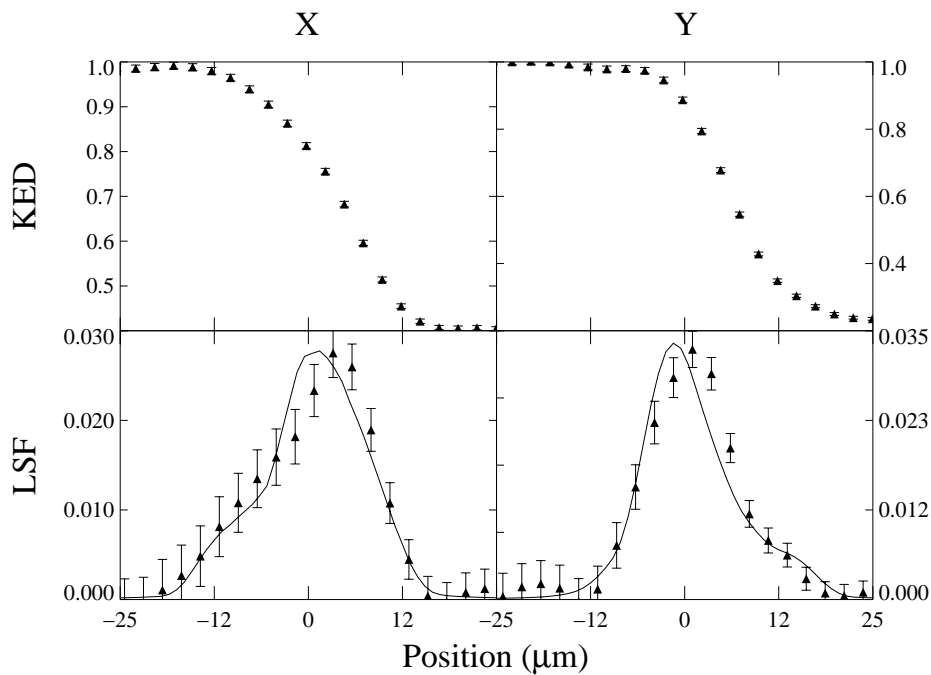


**Figure 6.** Knife edge distributions (KED) and derived line spread functions (LSF) associated with the return spot from the flight spare mirror in the laboratory image test setup in X (left column) and Y (right column). The solid line is the OSAC model prediction.

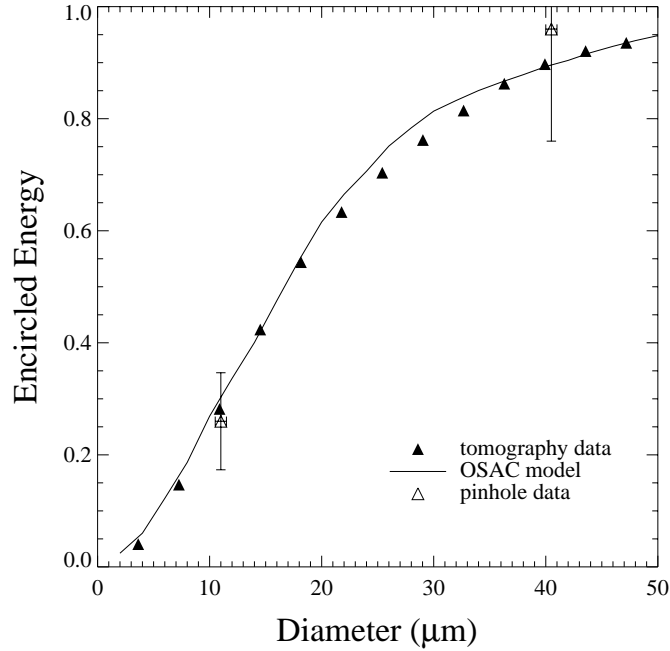


**Figure 7.** Encircled energy (EE) measurements derived from knife edge distributions via tomography for the flight spare mirror in the JHU laboratory image test setup at 184.9 nm (solid triangles). Statistical,  $1-\sigma$  errors are smaller than the plotting symbols. The solid line represents the OSAC EE prediction. Also shown are pinhole EE measurements (open triangles). Error bars reflect uncertainty in pinhole diameter and an estimate of systematic errors in the comparison of these measurements with the tomography EE data (i.e. positioning of the pinholes in X, Y and focus).

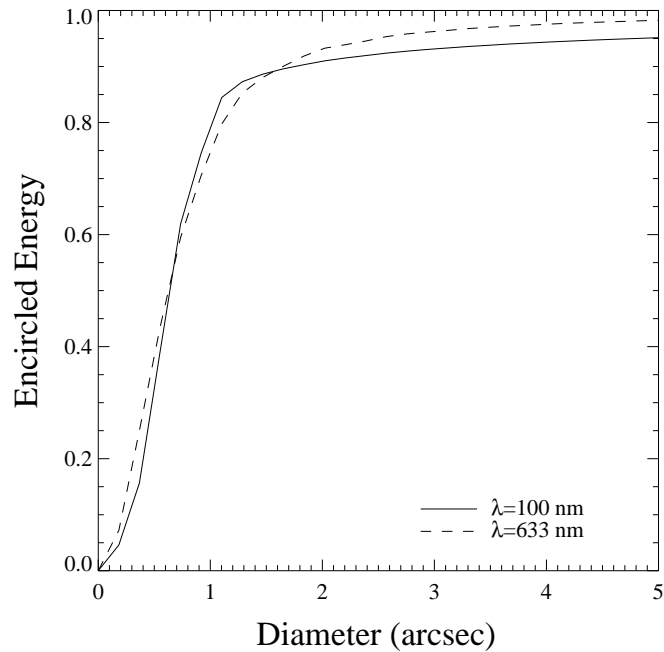


**Figure 8.** OSAC model EE prediction at 100.0 and 633.0 nm for the flight spare mirror in single pass.

## REFERENCES

1. D. J. Sahnou, S. D. Friedman, H. W. Moos, J. C. Green, and O. H. W. Siegmund, "Preliminary performance estimates for the Far Ultraviolet Spectroscopic Explorer (FUSE)," *Proc. SPIE* **3356**, pp. 552–560, 1998.
2. E. Wilkinson, J. C. Green, S. N. Osterman, K. R. Brownsberger, and D. J. Sahnou, "Integration, alignment, and initial performance results of the *Far Ultraviolet Spectroscopic Explorer* (FUSE) spectrograph," *Proc. SPIE* **3356**, pp. 18–29, 1998.
3. O. H. W. Siegmund, M. Gummin, J. Stock, G. Naletto, G. Gaines, R. Raffanti, J. Hull, R. Abiad, T. Rodriguez-Bell, T. Magoncelli, P. Jelinsky, W. Donakowski, and K. Kromer, "Performance of the double delay line microchannel plate detectors for the Far Ultraviolet Spectroscopic Explorer," *Proc. SPIE* **3114**, pp. 283–294, 1997.
4. M. J. Kennedy, S. D. Friedman, R. H. Barkhouser, J. Hampton, and P. Nikulla, "Design of the Far Ultraviolet Spectroscopic Explorer mirror assemblies," *Proc. SPIE* **2807**, pp. 172–183, 1996.
5. S. J. Conard, K. W. Redman, R. H. Barkhouser, and J. A. Johnson, "Optical alignment of the Far Ultraviolet Spectroscopic Explorer," *Proc. SPIE* **3765**, 1999 (this volume).
6. C. Oliveira, K. Retherford, S. J. Conard, R. H. Barkhouser, and S. D. Friedman, "Aging studies of LiF coated optics for use in the far ultraviolet," *Proc. SPIE* **3765**, 1999 (this volume).
7. T. T. Saha, D. B. Leviton, and P. Glenn, "Performance of ion-figured silicon carbide SUMER telescope mirror in the vacuum ultraviolet," *Appl. Opt.* **35**, pp. 1742–1750, 1996.
8. J. E. Harvey, *Final Report for FUSE Telescope Performance Predictions*, Consulting Agreement under NASA Con. NAS5-32985, (Johns Hopkins University, Baltimore, Md., 1996).
9. R. J. Noll, P. Glenn, and J. F. Osantowski, "Optical surface analysis code (OSAC)," in *Scattering in Optical Materials II*, S. Musikant, ed., *Proc. Soc. Photo-Opt. Instrum. Eng.* **62**, pp. 78–82, 1983.
10. J. E. Harvey and A. Kotha, "Scattering effects from residual optical fabrication errors," *Proc. SPIE* **2576**, pp. 155–174, 1995.
11. T. T. Saha, *Optical Surface Analysis Code (OSAC), User's Manual*, (Goddard Space Flight Center, Greenbelt, Md., 1993).
12. J. B. Houston, C. J. Buccini, and P. K. O'Neill, "A laser unequal path interferometer for the optical shop," *Appl. Opt.* **6**, pp. 1237–1242, 1967.
13. R. H. Barkhouser and R. G. Ohl, "Interferometric alignment and figure testing of large (0.5 m) off-axis parabolic mirrors in a challenging cleanroom environment," *Proc. SPIE* **3782**, 1999.
14. R. G. Ohl, R. H. Barkhouser, M. J. Kennedy, and S. D. Friedman, "Assembly and test-induced distortions of the FUSE mirrors — lessons learned," *Proc. SPIE* **3356**, pp. 854–865, 1998.
15. P. Glenn, "Lambda-over-thousand metrology results for steep spheres using a curvature profiling technique," in *Advanced Optical Manufacturing and Testing II*, V. J. Doherty, ed., *Proc. Soc. Photo-Opt. Instrum. Eng.* **1531**, pp. 54–61, 1991.
16. R. N. Bracewell, *Two-Dimensional Imaging*, Prentice-Hall, Inc., Englewood Cliffs, 1995.
17. M. C. Ruda, *Understanding Optical Alignment Techniques*, class notes from College of Engineering, University of Wisconsin-Madison, Boston, Mass., 1995.
18. P. Glenn, "Space Telescope performance prediction using the optical surface analysis code (OSAC)," *Opt. Eng.* **25**, pp. 1026–1033, 1986.
19. A. N. Cha, D. J. Sahnou, and H. W. Moos, "Processing and interpretation of pre-flight FUSE spectra," *Proc. SPIE* **3765**, 1999 (this volume).